

**Supporting Information for “Stabilization of AgI’s polar surfaces by the aqueous environment, and its implications for ice formation”**

Thomas Sayer<sup>1</sup> and Stephen J. Cox<sup>1, a)</sup>

*Department of Chemistry, University of Cambridge, Lensfield Road,  
Cambridge CB2 1EW, United Kingdom*

(Dated: 12 June 2019)

In this supporting information, we show that while using a ‘mirrored slab’ geometry may remove the net dipole of the simulation cell, it does not provide polarity compensation. A derivation of the CNC conditions is presented in the case that  $R_1 \neq R_2$ , which is the relevant case for AgI. We also present results not included in the main article for various combinations of fields and slab mobility, as well as results using different force fields and cell sizes. Finally, we give values of the parameters used in nonelectrostatic interactions.

---

<sup>a)</sup>Electronic mail: [sjc236@cam.ac.uk](mailto:sjc236@cam.ac.uk)

## I. MIRRORED SLAB GEOMETRY: REMOVING THE NET DIPOLE VS. POLARITY COMPENSATION

In the main article, we compared the behavior of AgI in contact with pure H<sub>2</sub>O at  $D_z = 0$  against simulations performed at  $D_{\text{CNC}}$  and  $E_{\text{CNC}}$ . Recall that the Hamiltonian for  $D_z = 0$  is equivalent to the commonly used Yeh-Berkowitz correction,<sup>1</sup> which adds a force  $F_{z,i} = -4\pi q_i P_z$  to each particle  $i$  in the simulation cell. In those simulations, the system comprised a single AgI slab immersed in H<sub>2</sub>O. We found a stark contrast in the behavior of the system under CNC conditions versus at  $D_z = 0$ , with a large potential drop of  $\Delta_{\text{xtl}}\phi = -46.2$  V across the crystal slab in the case of the latter. As the force applied by the YB correction is proportional to the net dipole of the simulation cell, another approach that has been taken is to use a ‘mirrored slab’ geometry, in which two slabs are used in the simulation, positioned in such a way that their dipoles cancel. If the net polarization of the simulation cell vanishes on average, and standard tin-foil boundary conditions are used, then we argue that this is equivalent on average to the  $D_z = 0$  ensemble. This is because tin foil boundary conditions correspond to the  $E_z = 0$  ensemble, giving  $\langle D_z \rangle_{E_z} = E_z + 4\pi \langle P \rangle_{E_z} = 0$ . We therefore do not expect the mirrored slab geometry to enforce CNC conditions.

To test the above hypothesis, we have performed a simulation with  $L_z = 21.75$  nm. An immobile AgI crystal is placed with its lowermost Ag-(0001) face at  $z = -7.42$  nm and its uppermost I-(000 $\bar{1}$ ) face at  $z = -4.33$  nm. A second crystal is then placed such that its dipole points in the opposite direction, with its lowermost I-(000 $\bar{1}$ ) face at  $z = +4.33$  nm and its uppermost Ag-(0001) face at  $z = +7.42$  nm. In the region  $-4.33 < z < +4.33$  nm we placed 750 TIP4P/2005 water molecules. The remaining volume was occupied by vacuum. All other simulation settings are the same as outlined in the main article. The resulting electrostatic potential profile is shown in Fig. S1(a). We can see that the potential drop across each slab closely resembles that seen for the simulations presented in the main article at  $D_z = 0$ . Indeed, we find  $|\Delta_{\text{xtl}}\phi| \approx 46.2$  V/nm in excellent agreement with the  $D_z = 0$  result presented in Fig. 3. We have also performed the simulations with the polarity of the AgI crystals reversed, such that water is in contact with the Ag-(0001) faces instead, and again find  $|\Delta_{\text{xtl}}\phi| \approx 46.2$  V/nm, see Fig. S1(b). These results clearly demonstrate that removing the net dipole of the simulation cell is not the same as providing polarity compensation.<sup>2</sup> As in the  $D_z = 0$  ensemble, the mobile slab is unstable in this mirrored slab

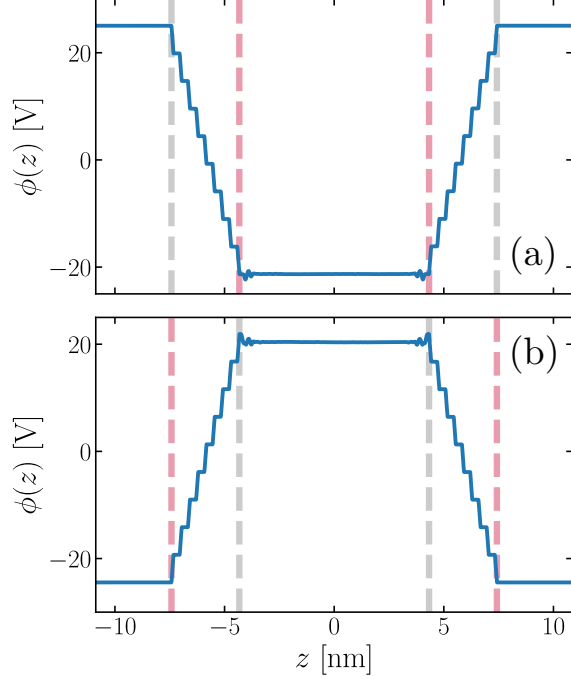


FIG. S1. Electrostatic potential profile  $\phi(z)$  obtained from the mirrored slab geometry at  $E_z = 0$ . The dashed silver and pink lines indicate the positions of the Ag-(0001) and I-(000 $\bar{1}$ ) surfaces respectively. The region  $-4.33 < z < +4.33$  nm is occupied by water, and the remaining volume ( $|z| > 7.42$  nm) is occupied by vacuum. As in the single slab geometry at  $D_z = 0$ , we find  $|\Delta_{\text{xtl}}\phi| \approx 46.2$  V/nm. In (a), the AgI crystals are arranged such that the I-(000 $\bar{1}$ ) faces are in contact with water, whereas in (b), the Ag-(0001) faces are in contact with water.

geometry [see Fig. 4(a)]. Moreover, we also find that the structure of water is similar to that at  $D_z = 0$ , as shown by the bond orientation statistics in Fig. S2(a). In Fig. S2(b) we also show the charge density profile  $\rho_q(z) = (L_x L_y)^{-1} \sum_i q_i \delta(z - z_i)$  close to one of the Ag-(0001) interfaces. Results are also shown for a single slab geometry with different fields and slab mobility, for comparison.

## II. DERIVATION OF THE CNC CONDITIONS

Consider the system shown schematically in Fig. S3, which comprises a polar crystal surrounded on either side by an aqueous electrolyte solution. The system is placed under three dimensional periodic boundary conditions, however, for the ensuing discussion, we are only concerned with the periodicity in the direction normal to the crystal's surfaces. The

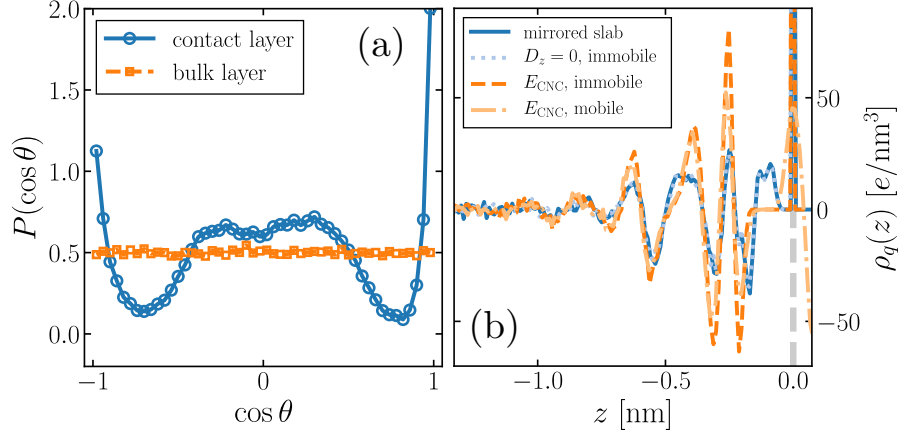


FIG. S2. (a) Bond orientation statistics in the mirrored slab geometry with water in contact with Ag-(0001) [see Fig. S1 (b)]. The results are consistent with the  $D_z = 0$  ensemble [see Fig. 5 (c)]. A value of  $\cos\theta = -1$  indicates a bond directed away from the surface, and  $\cos\theta = +1$  indicates a bond directed toward the surface. (b) Charge density profile  $\rho_q(z)$  from the Ag-(0001) interface. The  $z$ -coordinate has been shifted such that the Ag-(0001) interface is located at  $z = 0$ , and the liquid extends to  $z < 0$ . Results are shown for different simulation geometries and fields, as indicated by the legend.

length of the periodic supercell in this direction—which we take to be the  $z$  direction—is  $L_z$ . We consider the ‘insulator centered cell’ (ICS) where the crystal is centered at  $z = 0$ , and the cell spans  $-L_z/2 < z < L_z/2$ . The crystal is made up of  $n + 1$  planes of ions, each with a surface charge density  $\pm\sigma_0$ . ( $n$  is an odd integer.) As the crystal is a dielectric material, it can sustain finite electric fields in its interior. Here, we assume the field alternates between values  $E_1$  and  $E_2$  between the different ionic planes, as shown in Fig. S3. We have also assumed that the dielectric constant  $\epsilon_{\text{xtl}}$  is constant throughout the material. On the other hand, the surrounding electrolyte is a conductor, and the electric field in its interior strictly vanishes. In other words, the electrolyte screens the crystal’s surface charge. This screening induces planes of surface charge density  $\pm\sigma$  near the surface of the crystal, and the regions between these planes and the crystal are referred to as the Helmholtz layers. The electric field in the Helmholtz layer is denoted  $E_H$ , and its dielectric constant by  $\epsilon_H$ . As the electric displacement field must be continuous across the boundary separating the Helmholtz layer and the electrolyte,  $E_H \neq 0$  implies a finite polarization in the electrolyte. [This can be seen most readily by considering  $4\pi P = \lim_{\epsilon \rightarrow \infty} \epsilon^{-1}(\epsilon - 1)D$ .] An important implication of this

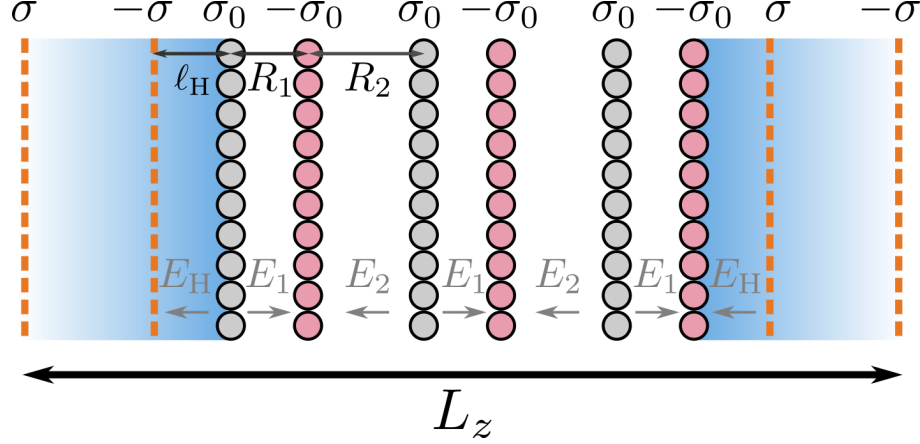


FIG. S3. Schematic of the continuum model used in the derivation of the CNC conditions. As in the main article (Fig. 1), the crystal comprises alternating layers with charge density  $\pm\sigma_0$ .  $E_1$  and  $E_2$  are the electric fields between layers in the crystal (assumed to have constant dielectric constant  $\epsilon_{\text{xtl}}$ ), with respective polarizations  $P_1$  and  $P_2$ .  $E_H$  is the electric field in the Helmholtz layer (situated a distance  $\ell_H$  from the crystal), which also has a polarization  $P_H$ . The leftmost and rightmost orange dashed lines indicate the cell boundaries. Due to the uniform polarization in the electrolyte, there are formally charge densities  $\pm\sigma$  at these boundaries.

is that there are formally surface charge densities of  $\pm\sigma$  at the boundaries of the simulation cell (see Fig. S3).

This configuration of charges produces dielectric polarization in each continuum region that alters the net charge at the boundaries. It is these net charges that determine the dipole moment. Explicitly they are,

$$\begin{aligned}\sigma_1 &= \sigma_0 - P_H - P_1, \\ \sigma_2 &= \sigma_0 - P_1 - P_2, \\ \sigma_H &= \sigma - P_H.\end{aligned}$$

The dipole moment of the simulation cell is then,

$$P_{z,\text{cell}} = \frac{1}{L} \sum_i \sigma_i z_i. \quad (\text{S1})$$

Performing this sum leads to,

$$\begin{aligned}
LP_{z,\text{cell}} = & -\sigma_1 \left[ \left( \frac{n+1}{2} \right) R_1 + \left( \frac{n-1}{2} \right) R_2 \right] \\
& + \sigma_H \left[ 2\ell_H + \left( \frac{n+1}{2} \right) R_1 + \left( \frac{n-1}{2} \right) R_2 \right] \\
& + \sigma_2 \left( \frac{n-1}{2} \right) R_2.
\end{aligned} \tag{S2}$$

In the case that  $R_1 = R_2$ , Eq. S2 reduces to the result previously derived in Ref. 3.

One of the central themes of the main article was the notion of *polarity compensation*. In macroscopically sized crystals, this means that the average field  $E_{\text{xtl}} = -\Delta_{\text{xtl}}\phi/w$  across the crystal must vanish in order to avoid a divergent surface energy. Clearly, the potential drop across the slab is the sum of electric fields inside the slab, appropriately weighted by the width of each region,

$$wE_{\text{xtl}} = \left( \frac{n+1}{2} \right) R_1 E_1 - \left( \frac{n-1}{2} \right) R_2 E_2, \tag{S3}$$

where the width of the slab is given as

$$w = \left( \frac{n+1}{2} \right) R_1 + \left( \frac{n-1}{2} \right) R_2. \tag{S4}$$

By construction, at CNC the potential drop across the crystal is zero. This allows us to write,

$$(n+1)R_1 E_1 = (n-1)R_2 E_2. \tag{S5}$$

We now express the surface charge densities by applying the Maxwell displacement equations across the boundaries, resulting in the following set of simultaneous equations,

$$\epsilon_H E_H = 4\pi\sigma \tag{S6}$$

$$\epsilon_H E_H + \epsilon_{\text{xtl}} E_1 = 4\pi\sigma_0 \tag{S7}$$

$$\epsilon_{\text{xtl}} E_2 + \epsilon_{\text{xtl}} E_1 = 4\pi\sigma_0. \tag{S8}$$

We can solve Eq. S5 for  $E_1$  and then substitute it into Eq. S8 to find  $E_2$  in terms of  $R_1$ ,  $R_2$ ,  $\sigma_0$  and  $\epsilon_{\text{xtl}}$ . Solving the simultaneous equations S6–S8 ultimately yields,

$$\sigma_{\text{CNC}} = \frac{(n+1)R_1}{(n+1)R_1 + (n-1)R_2} \sigma_0, \tag{S9}$$

where we have added the subscript ‘CNC’ to acknowledge that this is the value of  $\sigma$  that ensures  $\Delta_{\text{xtl}}\phi = 0$ . We again note that for  $R_1 = R_2$  we recover the result obtained in Ref. 3.

We will now show how  $\sigma_{\text{CNC}}$  is related to  $D_{\text{CNC}}$ , the value of the electric displacement field that enforces CNC conditions. This was derived in Ref. 4 for the case  $R_1 = R_2$ . Here we generalize the result to  $R_1 \neq R_2$ . Ultimately we will find that the difference between the two scenarios manifests itself entirely in the value of  $\sigma_{\text{CNC}}$ . In other words, for the ICS geometry we will find,

$$D_{\text{CNC}} = -4\pi\sigma_{\text{CNC}}, \quad (\text{S10})$$

with the value of  $\sigma_{\text{CNC}}$  determined by Eq. S9. To demonstrate this, we note the Maxwell field equations across the boundaries,

$$E_{\text{H}} = 4\pi\sigma_{\text{H}} \quad (\text{S11})$$

$$E_{\text{H}} + E_1 = 4\pi\sigma_1$$

$$E_2 + E_1 = 4\pi\sigma_2.$$

We can use these to write  $P_{z,\text{cell}}$  given by Eq. S2 in terms of electric fields rather than surface charge densities,

$$4\pi LP_{z,\text{cell}} = -E_1 \left( \frac{n+1}{2} \right) R_1 + 2E_{\text{H}}\ell_{\text{H}} + E_2 \left( \frac{n-1}{2} \right) R_2. \quad (\text{S12})$$

Like the potential drop across the crystal, the total potential drop across the cell  $\Delta_{\text{cell}}\phi = -LE_z$  can itself be written as the sum of all electric fields, appropriately weighted by the widths of the regions they occupy. This leads to,

$$E_z = \frac{1}{L} \left[ E_1 \left( \frac{n+1}{2} \right) R_1 - 2\ell_{\text{H}}E_{\text{H}} - E_2 \left( \frac{n-1}{2} \right) R_2 \right], \quad (\text{S13})$$

allowing us to write,

$$4\pi P_{z,\text{cell}} = -E_z. \quad (\text{S14})$$

At this point it is important to realize that  $E_z$  is the Maxwell field and includes all possible contributions. Thus  $E_z$  comprises contributions from both the cell polarization *and* applied fields. In the current context, this manifests itself in the form of the induced charges  $\pm\sigma$  at the cell boundaries. *The full polarization must also include the charge induced at the boundaries of the supercell,*

$$4\pi P_z = -4\pi\sigma - E_z. \quad (\text{S15})$$

From the Maxwell relation  $D_z = E_z + 4\pi P_z$ , Eq. S10 follows immediately when enforcing CNC conditions.

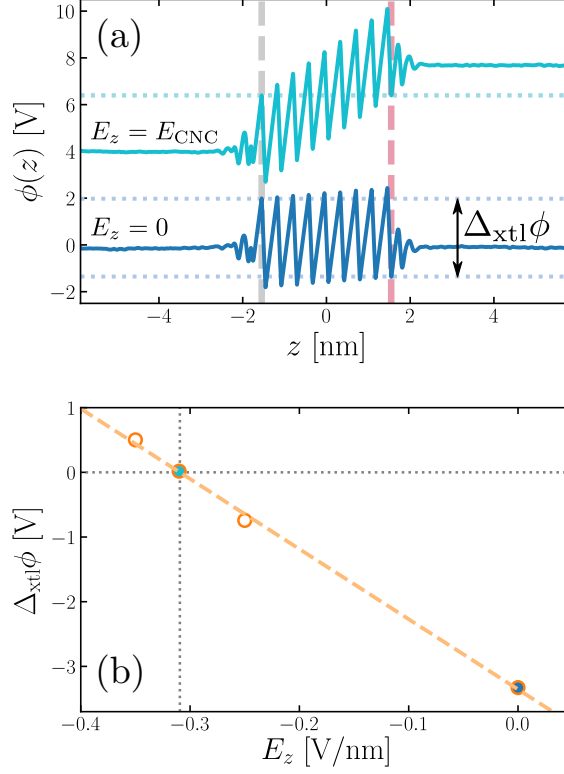


FIG. S4. Trial-and-error approach for locating  $E_{\text{CNC}}$ . (a)  $\phi(z)$  for  $E_z = 0 \text{ V/nm}$  (dark blue) and  $E_z = E_{\text{CNC}}$  (cyan). (See Fig. 2.) At  $E_z = 0 \text{ V/nm}$  there exists a potential drop  $\Delta_{\text{xtl}}\phi$  across the crystal, as indicated. (b)  $\Delta_{\text{xtl}}\phi$  vs  $E_z$  exhibits an approximately linear relationship, as indicated by the dashed line. The cyan and dark blue data points correspond to  $E_{\text{CNC}}$  and  $E_z = 0 \text{ V/nm}$ , respectively.

### III. ESTABLISHING CNC CONDITIONS UNDER CONSTANT $E_z$

In the main paper, we discussed the trial-and-error procedure for finding  $E_{\text{CNC}}$ . This is displayed pictorially in Fig. S4. To help orient the reader, Fig. S4(a) is a replica of Fig. 2. To find  $E_{\text{CNC}}$  we simply perform simulations at different values of  $E_z$  and measure the value of  $\Delta_{\text{xtl}}\phi$  that results. The value of  $E_{\text{CNC}}$  that causes  $\Delta_{\text{xtl}}\phi$  to vanish (or in practice, to be sufficiently small e.g.  $|\Delta_{\text{xtl}}\phi| < 0.2 \text{ V}$ ), is the value of  $E_{\text{CNC}}$ . In general this procedure is greatly facilitated by the approximately linear relation between  $\Delta_{\text{xtl}}\phi$  and  $E_{\text{CNC}}$ , which allows us to extrapolate to  $E_{\text{CNC}}$  with just a few data points. Results from a typical trial-and-error procedure are shown in Fig. S4(b).



#### IV. VALUES OF $E_z$ AND $D_z$ USED IN SIMULATIONS OF CNC CONDITIONS

We have performed a number of simulations with different values of  $E_z$  and  $D_z$  in order to approximate CNC conditions. The different values used are summarized in Table S1, where we also give the corresponding values of  $\Delta_{\text{xtl}}\phi$ . Due to relaxation of the  $\text{Ag}^+$  and  $\text{I}^-$  ions, in the case of the mobile slab there is no reason to expect the values of  $E_{\text{CNC}}$  and  $D_{\text{CNC}}$  to remain unchanged from those for the immobile crystal. For the  $\text{AgI} + \text{pure H}_2\text{O}$  system, we find that  $E_z = -0.56 \text{ V/nm}$  is a good approximation for  $E_{\text{CNC}}$  in both cases, but that  $D_{\text{CNC}}$  changes from  $D_z = -14.99 \text{ V/nm}$  to  $D_z = -15.74 \text{ V/nm}$ . For the  $\text{AgI} + \text{electrolyte}$  system, on the other hand, using the same value of  $E_z = -0.31 \text{ V/nm}$  for the immobile and mobile slab leads to a potential difference of  $\Delta_{\text{xtl}}\phi \approx +0.39 \text{ V}$  across the crystal in the latter case. This was the value used in the simulations of ice formation at  $E_{\text{CNC}}$  with a mobile slab. The average value of the electric displacement field at 298 K was found to be  $\langle D_z \rangle_{E_z=-0.31} \approx -15.88 \text{ V/nm}$ . Performing a simulation with a mobile slab at  $E_z = -0.26 \text{ V/nm}$  (which gives  $\Delta_{\text{xtl}}\phi \approx -0.04 \text{ V}$ ) gives  $\langle D_z \rangle_{E_z=-0.26} \approx -15.51 \text{ V/nm}$ , and this was the value used in the simulations of ice formation at  $D_{\text{CNC}}$  with a mobile slab. Nevertheless, we observe similar results between the two ensembles, suggesting that the  $\text{AgI}$  crystal—and ice formation in its presence—is sufficiently robust to such relatively small potential drops across the crystal, at least for the simulation cell sizes investigated in the main article. See e.g. Figs. S5-S10.

#### V. RESULTS NOT PRESENTED IN THE MAIN ARTICLE

In this section we give results not presented in the main article. Figs. S5–S8 show orientation statistics at  $\text{Ag-(0001)}$  for different combinations of fields, temperatures, and whether or not the slab is mobile. The reader is referred to the figure captions for details. Good agreement with those results presented in the main manuscript is seen in all cases. Figure S9 shows the number of ice-like molecules,  $N_{\text{ice}}$ , vs. time,  $t$ , in the absence of dissolved ions. To determine  $N_{\text{ice}}$ , we have used the CHILL+ algorithm.<sup>5</sup> As the crystal structure of  $\text{AgI}$  resembles that of ice, we have included the  $\text{Ag}^+$  and  $\text{I}^-$  ions in the analysis, and we have also shifted the  $y$  coordinates of the  $\text{Ag}^+$  and  $\text{I}^-$  ions by  $-0.2651 \text{ nm}$  to enhance

TABLE S1. Summary of  $E_z$  and  $D_z$  values used for the CNC simulations presented in the main article (reported in V/nm), along with corresponding  $\Delta_{\text{xtl}}\phi$  (reported in V). For the case of a mobile AgI slab in contact with NaCl electrolyte, these were performed at a value close to  $E_{\text{CNC}}$ , and have therefore been marked with an asterisk (see text).

| System                              | $E_{\text{CNC}}$ | $D_{\text{CNC}}$ | $\Delta_{\text{xtl}}\phi$ at $E_{\text{CNC}}$ | $\Delta_{\text{xtl}}\phi$ at $D_{\text{CNC}}$ |
|-------------------------------------|------------------|------------------|---|---|
| immobile AgI, pure H <sub>2</sub> O | -0.56            | -14.99           | -0.06   | +0.15   |
| immobile AgI, NaCl electrolyte      | -0.31            | -14.99           | +0.02   | +0.15   |
| mobile AgI, pure H <sub>2</sub> O   | -0.56            | -15.74           | -0.08   | +0.10   |
| mobile AgI, NaCl electrolyte        | -0.31*           | -15.51           | +0.39*  | -0.10   |

the performance of the algorithm at Ag-(0001). (This shifting is only performed during the CHILL+ analysis.) Figure S10 shows the corresponding plots for the electrolyte system. Both of these results are discussed in Sec. IIIB in the main article. In Fig. S11 we show snapshots from simulations ( $D_{\text{CNC}}$  and  $E_{\text{CNC}}$  for pure H<sub>2</sub>O in contact with AgI) in which ice formation is seen to occur at I-(000 $\bar{1}$ ) as well as Ag-(0001). We stress that ice formation is still seen to occur preferentially at Ag-(0001), even in the simulations shown in Fig. S11. Due to this preference for ice formation at Ag-(0001), all the results for  $P(\cos\theta)$  shown in the main article and in this supporting information have focused on the contact layer at this interface. In Fig. S12 we present  $P(\cos\theta)$  for the contact layer at I-(000 $\bar{1}$ ) from  $D_z = 0$ , and under CNC conditions. We see analogous behavior to that reported at the Ag-(0001), i.e., at  $D_z = 0$  no water molecules direct O-H bonds toward the negatively charged interface, whereas under CNC conditions, a significant proportion do. In Fig. S13, we present orientation statistics of water dipoles at Ag-(0001) for  $D_z = 0$  and at  $D_{\text{CNC}}$ . This is an alternative way of elucidating water's structure at the interface, rather than looking at statistics of O-H bonds.

All results presented so far have been obtained with the TIP4P/2005 water model,<sup>6</sup> and the Madrid model for the NaCl ions.<sup>7</sup> While we may expect the thermodynamics and kinetics of ice formation to depend sensitively on force field parameters, the CNC conditions have been derived from a continuum model (see Sec. II). We therefore expect the CNC conditions to be robust to the force field used for the water and dissolved ions. To demonstrate this, we

have performed simulations at 298 K using 864 SPC/E water<sup>8</sup> ( $q_{\text{O}} = -0.8476e$ ) and three Joung-Cheatham NaCl ion pairs<sup>9</sup> ( $q_{\text{NaCl}} = 1e$ ). The resulting  $\phi(z)$  for an immobile crystal are shown in Fig. S14, both for at  $D_z = 0$  and  $D_{\text{CNC}} = -14.99 \text{ V/nm}$ . At  $D_z = 0$ , we find  $|\Delta_{\text{xtl}}\phi| = 46.2 \text{ V}$ , while at  $D_{\text{CNC}}$  we find  $|\Delta_{\text{xtl}}\phi| = 0.15 \text{ V}$ . These are in excellent agreement with the results obtained with the TIP4P/2005 and Madrid models. In Fig. S15 we show the corresponding orientation statistics of O–H bonds at Ag-(0001). Similar behavior is observed compared to results obtained with the TIP4P/2005 and Madrid models.

In addition to being insensitive to the water and NaCl force field parameters, the CNC conditions also appear to be independent of  $L_x$  and  $L_y$ . Indeed, doubling the extent of the simulation cell in these dimensions while keeping  $L_z$  fixed (such that the system is four times as large) results in the  $\phi(z)$  profiles shown in Fig. S16. These results for the immobile crystal agree excellently with the those found in the main article (see Fig. 3). Importantly, the field in the solvent is the same for both simulation setups,  $E_{z,\text{solv}} \approx -0.39 \text{ V/nm}$ . This leads to similar structures as reported in the main article, as seen in Fig. S17. With such a large field in the solvent, we expect a similar proton ordered ice structure to form in this system too. For the mobile crystal, however, we have found that  $E_{\text{CNC}}$  changes slightly from  $-0.56 \text{ V/nm}$  to  $-0.55 \text{ V/nm}$ , whereas for the system studied in the main article, we found no discernible difference upon moving to a mobile crystal in the presence of pure water (see Table S1).

## VI. FURTHER SIMULATION DETAILS

As discussed in Sec. V of the main article, we used the reparametrized<sup>10</sup> PRV potential<sup>11</sup> to model AgI, as detailed in Ref. 12. To this end, we found it convenient to used a look-up table to compute non-electrostatic interactions for the PRV potential. These interactions take the form,

$$u_{\text{PRV}}(r) = \frac{H}{r^\eta} - \frac{C}{r^6} - \frac{P}{r^4} \quad (\text{S16})$$

where  $r$  is the interatomic separation, and  $H$ ,  $\eta$ ,  $C$  and  $P$  are parameters that take specific values for the different types of interactions (i.e.  $\text{Ag}^+-\text{Ag}^+$ ,  $\text{Ag}^+-\text{I}^-$  and  $\text{I}^--\text{I}^-$ ). Like all other non-electrostatic interactions, these were truncated and shifted at  $r = 10 \text{ \AA}$ .  $u_{\text{PRV}}$  was then tabulated with a spacing  $\Delta r = 0.02 \text{ \AA}$ . In Fig. S18(a) we show the *output* from LAMMPS of the interpolated potential, at a resolution  $\delta r \approx 0.015 \text{ \AA}$ . It is clear that the

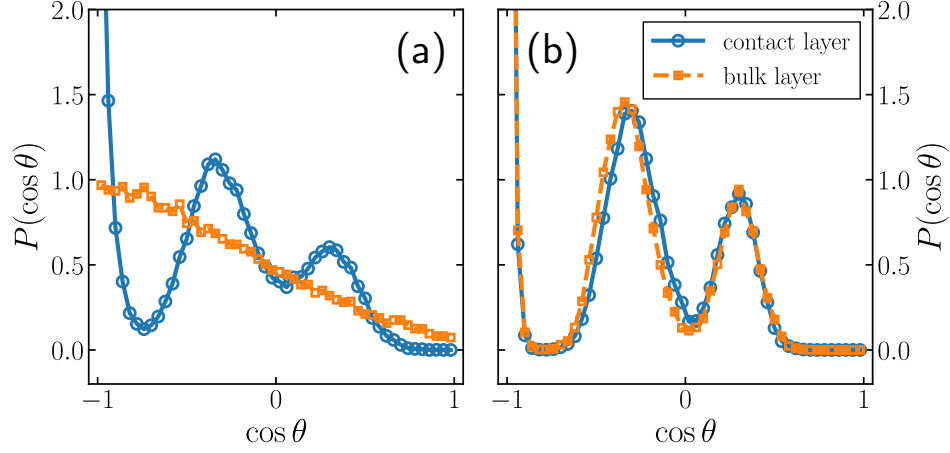


FIG. S5. Orientation statistics for pure H<sub>2</sub>O in contact with an immobile AgI crystal, at  $E_{\text{CNC}}$ . (a) Simulation performed at 298 K with water in its liquid state. (b) After ice formation at 242 K. Good agreement with the simulations performed at  $D_{\text{CNC}}$  is observed, see Figs. 5 (d) and 6 (d).

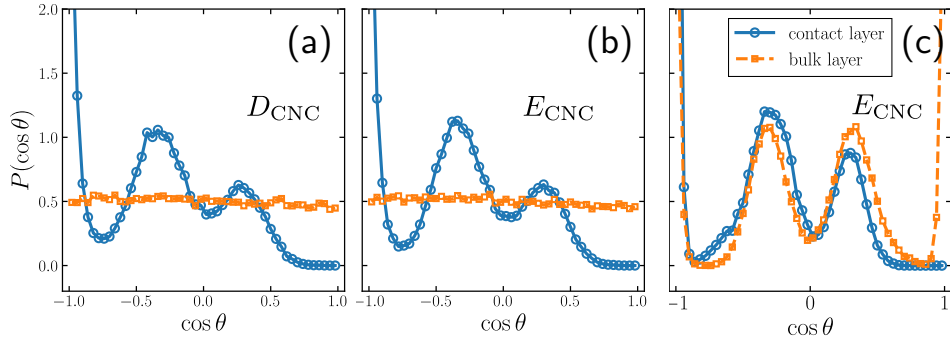


FIG. S6. Orientation statistics of water (NaCl electrolyte) in the contact layer and away from the crystal, in the presence of an immobile AgI crystal. Simulations at 298 K at (a)  $D_{\text{CNC}}$  and (b)  $E_{\text{CNC}}$ . In both cases, no orientation order is observed away from the surface. No water molecules in the contact layer direct O–H bonds toward the surface. (c) After ice formation at 242 K at  $E_{\text{CNC}}$ . These results are consistent with those seen at  $D_{\text{CNC}}$ , see Fig. 7 (b).

interpolation agrees well with the analytic form given by Eq. S16. In Fig. S18 (b) we show radial distribution functions  $g(r)$  between the different species obtained for molten AgI at 923 K (250 AgI ion pairs, in a cubic simulation box with dimension  $L = 26.1069 \text{ \AA}$ ). These appear to agree well with those reported by Bitrián and Trullàs.<sup>12</sup>

In Table S3 we report the parameters for the Lennard-Jones (LJ) interactions between

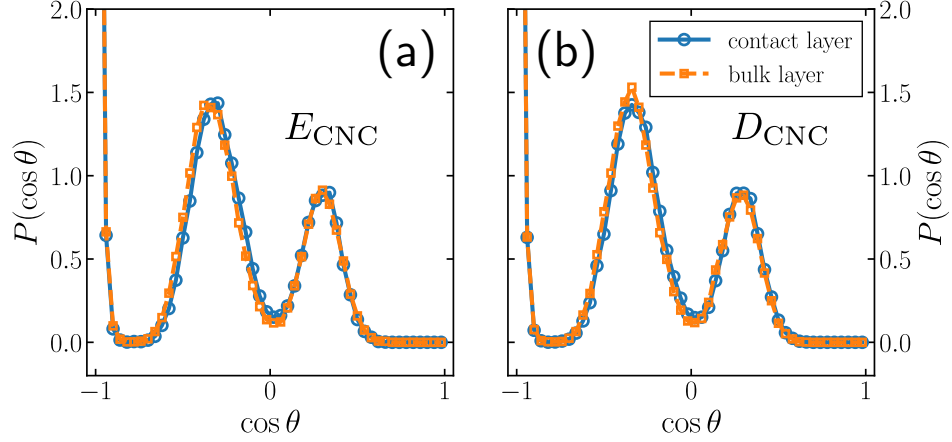


FIG. S7. Orientation statistics after ice formation for pure  $\text{H}_2\text{O}$  in the contact layer and away from the crystal, in the presence of a mobile AgI crystal. Simulations have been performed both at (a)  $E_{\text{CNC}}$  and (b)  $D_{\text{CNC}}$ . The results agree well with those presented in Fig. 6 (d), where an immobile AgI crystal was used.

TABLE S2. Parameters used in the PRV potential, see Eq. S16.  $\eta$  is dimensionless.  $H$ ,  $C$  and  $P$  are given in  $\text{eV } \text{\AA}^\eta$ ,  $\text{eV } \text{\AA}^4$  and  $\text{eV } \text{\AA}^6$ , respectively.

| interaction pair          | $\eta$ | $H$    | $P$  | $C$  |
|---------------------------|--------|--------|------|------|
| $\text{Ag}^+-\text{Ag}^+$ | 11     | 0.16   | 0    | 0    |
| $\text{Ag}^+-\text{I}^-$  | 9      | 1310.0 | 14.9 | 0    |
| $\text{I}^--\text{I}^-$   | 7      | 5328.0 | 29.8 | 84.5 |

different species, where the LJ potential is,

$$u_{\text{LJ}}(r) = 4\epsilon_{\text{LJ}} \left[ \left( \frac{\sigma_{\text{LJ}}}{r} \right)^{12} - \left( \frac{\sigma_{\text{LJ}}}{r} \right)^6 \right]. \quad (\text{S17})$$

Interactions between  $\text{H}_2\text{O}$ ,  $\text{Na}^+$  and  $\text{Cl}^-$  use the Madrid model.<sup>7</sup> Interactions between  $\text{H}_2\text{O}$ ,  $\text{Ag}^+/\text{I}^-$  use the parameters of Hale and Kiefer,<sup>13</sup> as reported by Fraux and Doye.<sup>14</sup> Remaining interactions between  $\text{Na}^+/\text{Cl}^-$  and  $\text{Ag}^+/\text{I}^-$  were computed using Lorentz-Berthelot mixing rules. The hydrogen atoms of the water molecules do not interact via the LJ potential, and have been omitted from Table S3.

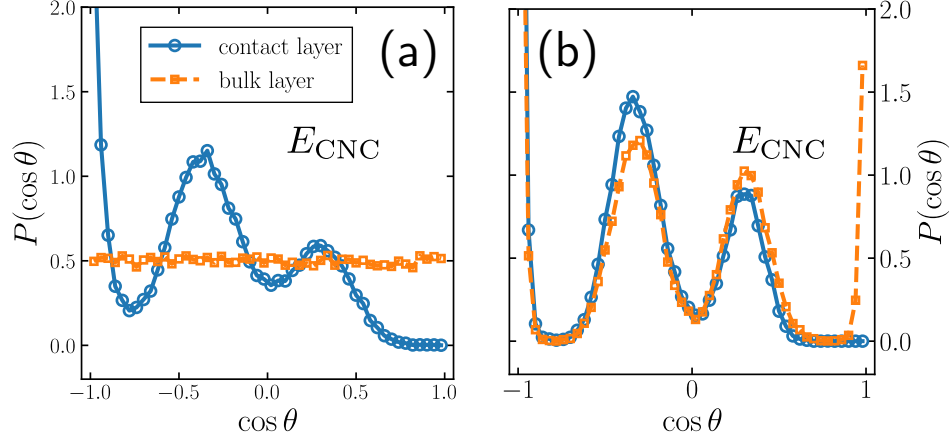


FIG. S8. Orientation statistics of water (NaCl electrolyte) in contact with a mobile AgI crystal, at  $E_{\text{CNC}}$ . (a) Simulation performed at 298 K with water in its liquid state. Good agreement with the simulations performed with an immobile slab is observed, see Fig. S6. (b) After ice formation at 242 K. Again, good agreement is seen with the immobile slab simulations. Moreover, the results are also consistent with those performed at  $D_{\text{CNC}}$ , see Fig. 7 (b).

TABLE S3. LJ interaction parameters ( $\epsilon_{\text{LJ}}, \sigma_{\text{LJ}}$ ) reported to four decimal places.  $\epsilon_{\text{LJ}}$  is reported in kcal/mol, and  $\sigma_{\text{LJ}}$  is reported in Ångstrom. ‘—’ indicates no LJ interaction is specified between this pair of species.

|                 | O                | Na <sup>+</sup>  | Cl <sup>-</sup>  | Ag <sup>+</sup>  | I <sup>-</sup>   |
|-----------------|------------------|------------------|------------------|------------------|------------------|
| O               | (0.1852, 3.1589) | (0.1896, 2.5134) | (0.0148, 4.2687) | (0.5467, 3.1710) | (0.6220, 3.3420) |
| Na <sup>+</sup> |                  | (0.3519, 2.2174) | (0.3439, 2.9051) | (0.7536, 2.7002) | (0.8574, 2.8712) |
| Cl <sup>-</sup> |                  |                  | (0.0184, 4.8491) | (0.1723, 4.0161) | (0.1960, 4.1871) |
| Ag <sup>+</sup> |                  |                  |                  | —                | —                |
| I <sup>-</sup>  |                  |                  |                  |                  | —                |

## REFERENCES

- <sup>1</sup>I.-C. Yeh and M. L. Berkowitz, J. Chem. Phys. **111**, 3155 (1999).
- <sup>2</sup>J. Goniakowski, F. Finocchi, and C. Noguera, Rep. Prog. Phys. **71**, 016501 (2008).
- <sup>3</sup>T. Sayer, C. Zhang, and M. Sprik, J. Chem. Phys. **147**, 104702 (2017).

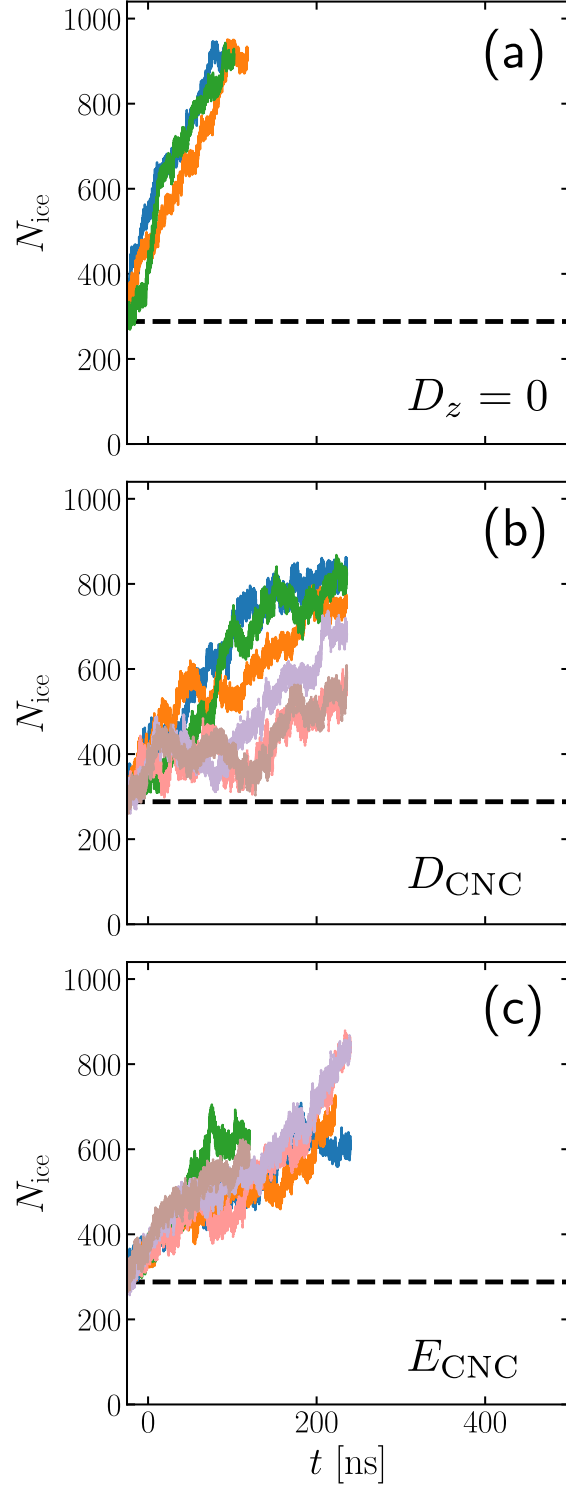


FIG. S9.  $N_{\text{ice}}$  vs  $t$  for pure  $\text{H}_2\text{O}$  in contact with AgI. Blue, green and orange lines indicate the results obtained with an immobile AgI crystal, while purple, brown and pink indicate results obtained with a mobile AgI crystal. (a) Simulations performed at  $D_z = 0$  (immobile slab only). (b) Simulations performed at  $D_{\text{CNC}}$ . (c) Simulations performed at  $E_{\text{CNC}}$ . The black dashed line indicates the number of AgI ions, which have also been included in the CHILL+ analysis.

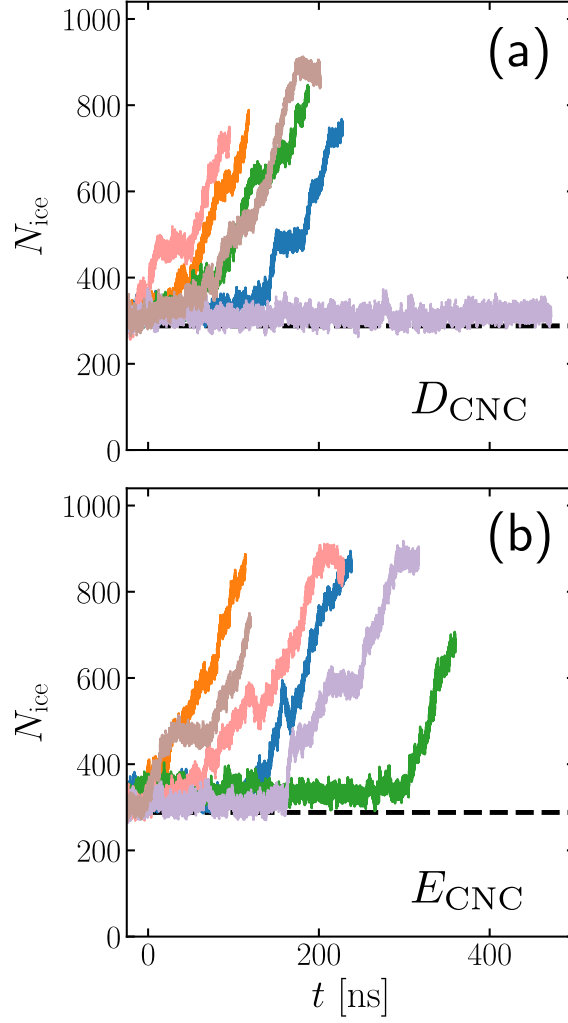


FIG. S10.  $N_{\text{ice}}$  vs  $t$  for NaCl electrolyte in contact with AgI. Color scheme as in Fig. S9. (a) Simulations performed at  $D_{\text{CNC}}$ . (b) Simulations performed at  $E_{\text{CNC}}$ . In contrast to the pure water system, ice formation in the presence of ions appears to be preceded by an induction time followed by rapid growth. The black dashed line indicates the number of AgI ions, which have also been included in the CHILL+ analysis.

<sup>4</sup>T. Sayer, M. Sprik, and C. Zhang, J. Chem. Phys. **150**, 041716 (2019).

<sup>5</sup>A. H. Nguyen and V. Molinero, J. Phys. Chem. B **119**, 9369 (2014).

<sup>6</sup>J. L. Abascal and C. Vega, J. Chem. Phys. **123**, 234505 (2005).

<sup>7</sup>A. Benavides, M. Portillo, V. Chamorro, J. Espinosa, J. Abascal, and C. Vega, J. Chem. Phys. **147**, 104501 (2017).

<sup>8</sup>H. J. C. Berendsen, J. R. Grigera, and T. P. Straatsma, J. Phys. Chem. **91**, 6269 (1987).



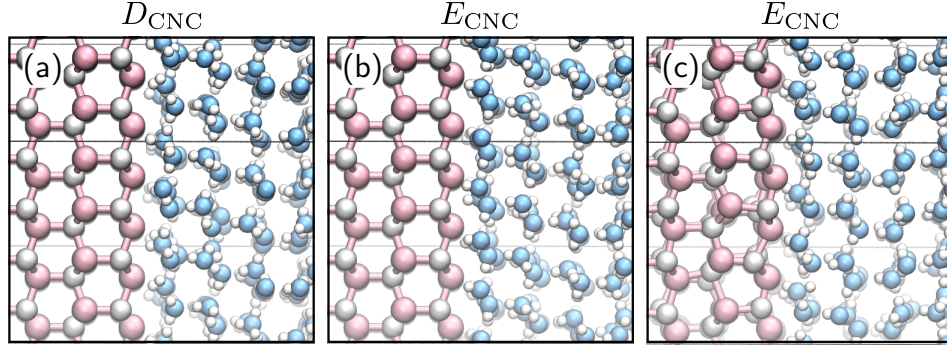


FIG. S11. Examples of ice formation at  $I-(000\bar{1})$  for pure  $H_2O$  in contact with  $AgI$ . We stress that ice formation occurs preferentially at  $Ag-(0001)$ , even in the simulations shown in this figure. (a) and (b) show snapshots from simulations performed at  $D_{CNC}$  and  $E_{CNC}$ , respectively, with an immobile crystal. (c) Snapshot from simulation performed at  $E_{CNC}$  with a mobile crystal.

<sup>9</sup>I. S. Joung and T. E. Cheatham III, J. Phys. Chem. B **112**, 9020 (2008).

<sup>10</sup>F. Shimojo and M. Kobayashi, J. Phys. Soc. Jpn. **60**, 3725 (1991).

<sup>11</sup>M. Parrinello, A. Rahman, and P. Vashishta, Phys. Rev. Lett. **50**, 1073 (1983).

<sup>12</sup>V. Bitrián and J. Trullàs, J. Phys. Chem. B **112**, 1718 (2008).

<sup>13</sup>B. N. Hale and J. Kiefer, J. Chem. Phys. **73**, 923 (1980).

<sup>14</sup>G. Fraux and J. P. Doye, J. Chem. Phys. **141**, 216101 (2014).

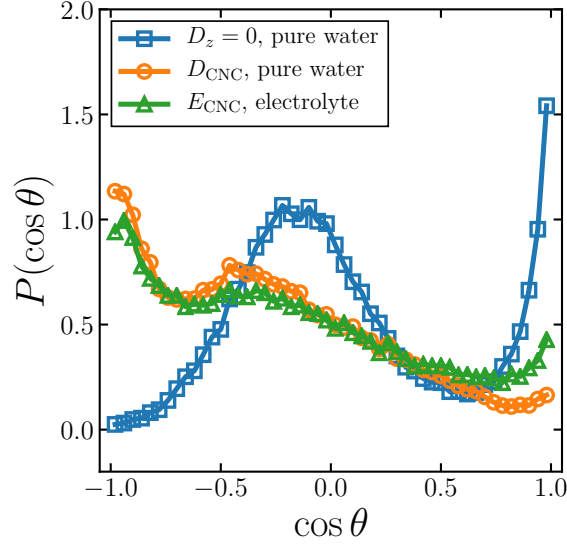


FIG. S12. Orientation statistics of water at I-(000 $\bar{1}$ ), at  $D_z = 0$  and under CNC conditions (see legend). The results are analogous to those at Ag-(0001): At  $D_z = 0$ , essentially no water molecules direct O–H bonds toward the surface, whereas under CNC conditions, many water molecules do direct O–H bonds toward the negatively charged surface. Note that in contrast to our analysis at Ag-(0001),  $\cos \theta = -1$  indicates a bond directed toward the surface, and  $\cos \theta = +1$  indicates a bond directed away from the surface.

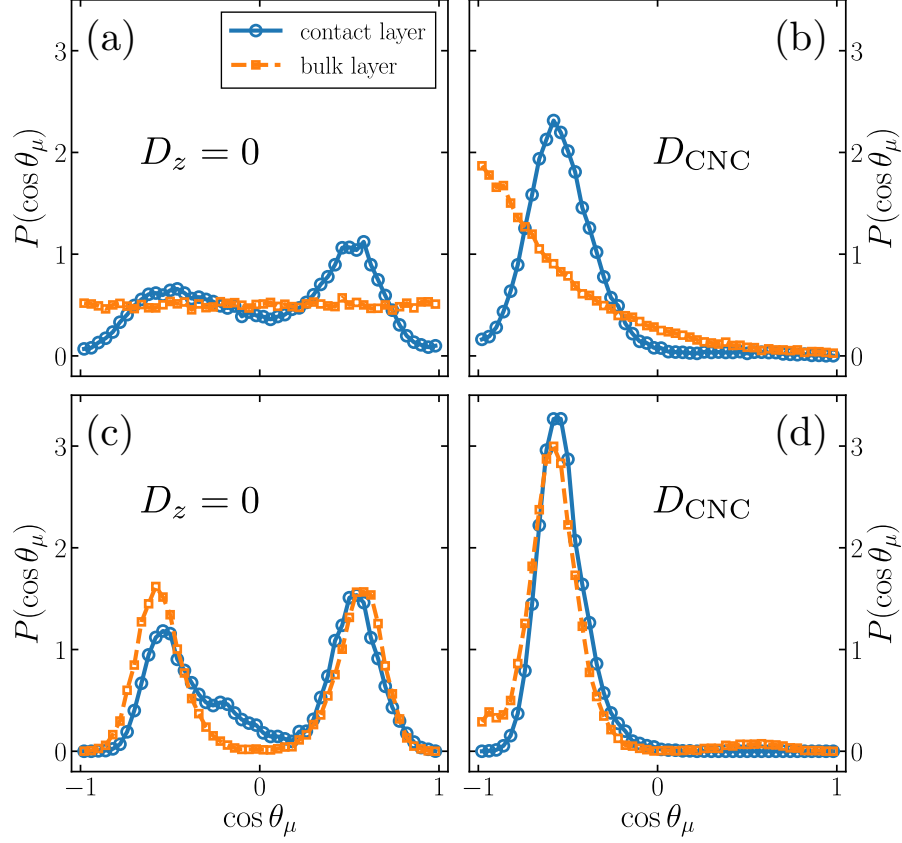


FIG. S13. Orientation statistics of water dipoles at Ag-(0001).  $\theta_\mu$  is the angle between a water dipole and the  $z$ -axis of the simulation cell. (a) and (b) show results for liquid water at 298 K for  $D_z = 0$  and at  $D_{\text{CNC}}$ , respectively. (c) and (d) show results after ice formation at 242 K for  $D_z = 0$  and at  $D_{\text{CNC}}$ , respectively. A value of  $\cos \theta = -1$  indicates a dipole directed away from the surface, and  $\cos \theta = +1$  indicates a dipole directed toward the surface. All results used an immobile crystal.

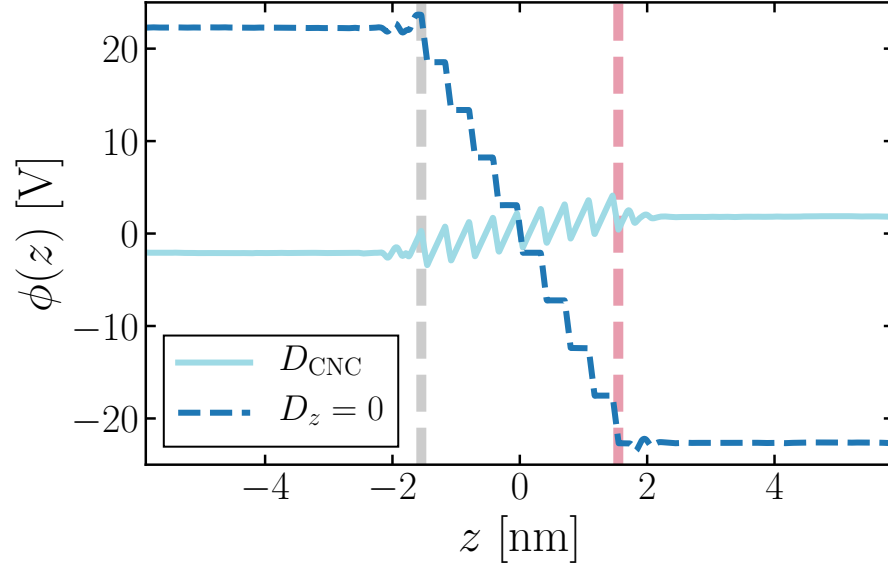


FIG. S14.  $\phi(z)$  using SPC/E water and Joung-Cheatham NaCl (three ions pairs) at 298 K. The striking similarity to the results obtained with TIP4P/2005 and the Madrid model demonstrate the robustness of the CNC conditions to the underlying atomic model of the electrolyte. Results have been obtained with an immobile crystal.

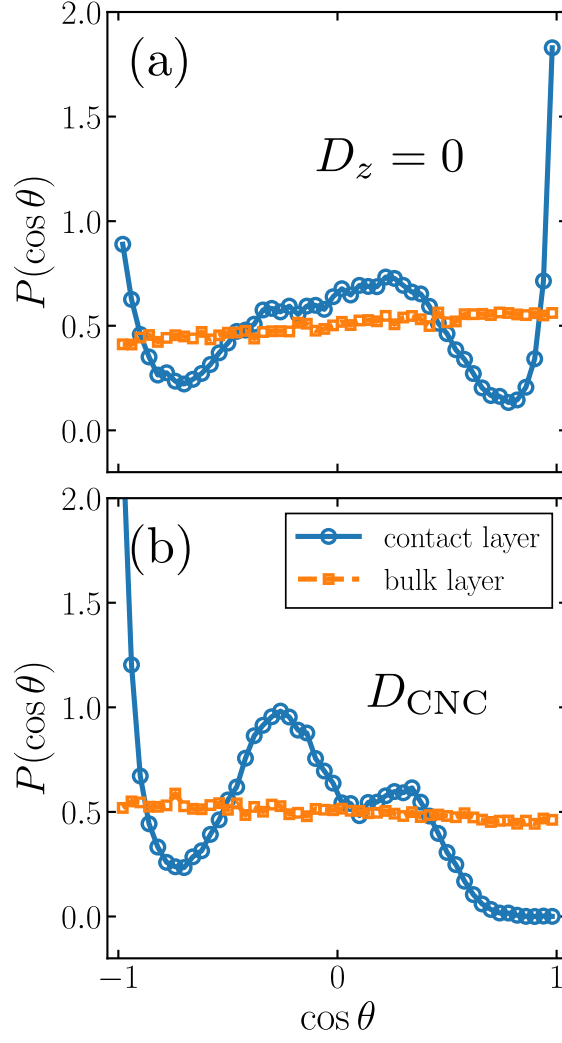


FIG. S15. Orientation statistics of water (NaCl electrolyte) in contact with an immobile AgI crystal, at 298 K. Results have been obtained with the SPC/E and Joung-Cheatham force fields.

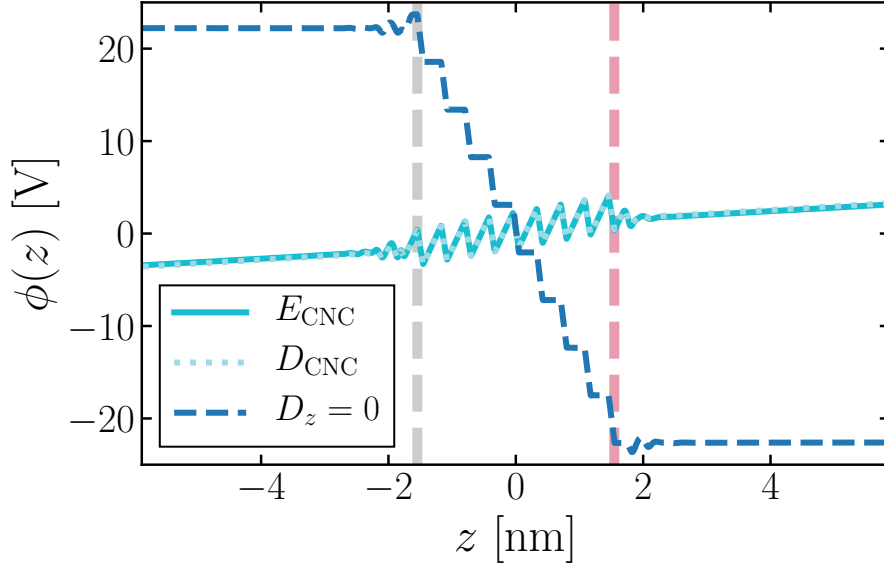


FIG. S16. Comparing  $\phi(z)$  from different ensembles for AgI ( $n = 17$ ) in contact with pure water at 298 K, with the system doubled in the  $x$  and  $y$  dimensions. At  $D_z = 0$  we find  $\Delta_{\text{xtl}}\phi \approx -46.2$  V. At  $E_{\text{CNC}}$  we find  $\Delta_{\text{xtl}}\phi \approx -0.04$  V, and  $|E_{z,\text{solv}}| \approx 0.39$  V/nm. The result obtained at  $D_{\text{CNC}} = -14.99$  V/nm (dotted line) agrees well with the  $E_{\text{CNC}}$  result.

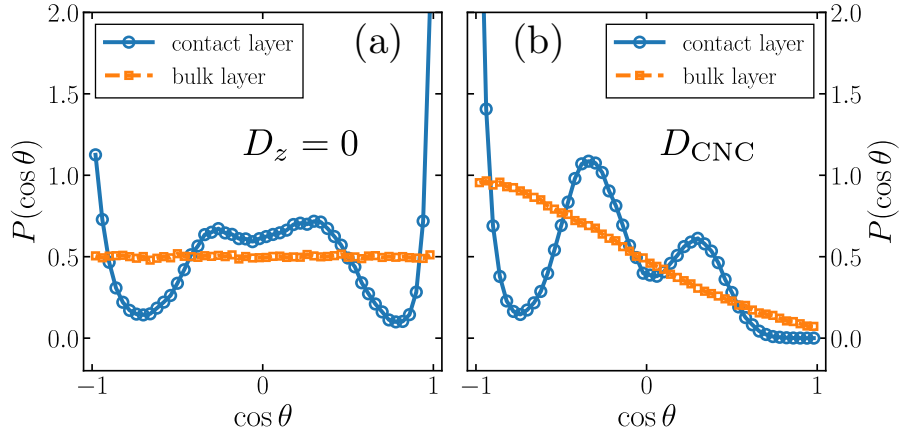


FIG. S17. Bond orientation statistics at 298 K for a system at whose extent in  $x$  and  $y$  has been doubled. (a) and (b) show  $P(\cos \theta)$  at  $D_z = 0$  and  $D_{\text{CNC}}$ , respectively, both for water molecules in the contact layer (blue circles) and in bulk solvent (orange squares).  $\cos \theta = +1$  and  $\cos \theta = -1$  indicate O–H bonds directed immediately toward and away from Ag-(0001), respectively. All results have been obtained with an immobile crystal.

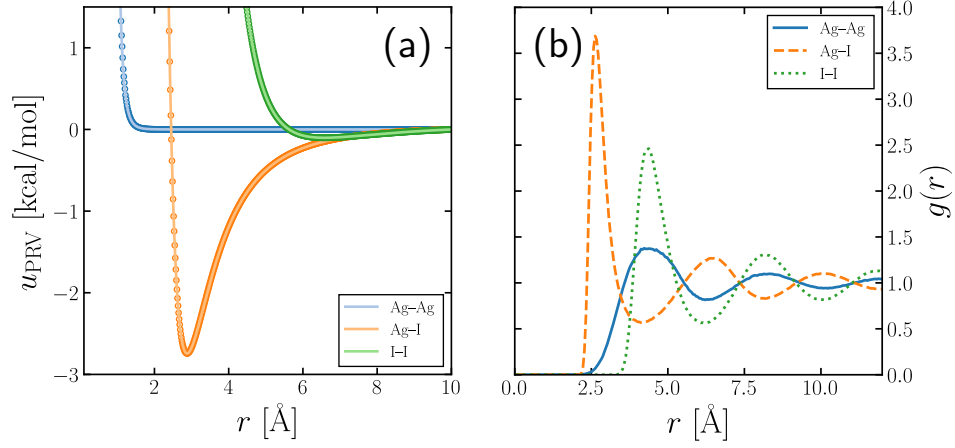


FIG. S18. (a) Non-electrostatic portion of  $u_{\text{PRV}}$  vs interatomic separation. The symbols have been output from LAMMPS at a resolution of approximately 0.0015 nm, while the solid lines show the analytic form of the PRV potential (truncated and shifted at  $r = 1$  nm). (b) Radial distribution functions from simulations of molten AgI at 923 K. These appear to agree well with those reported in Ref 12.